DESIGN AND EXPERIMENTAL EVALUATION OF A HIGH-SPEED, DIRECTLY-COUPLED, MULTI-MEGAWATT PERMANENT-MAGNET MACHINE

by

Cassandra Bailey

Project Engineer

Daniel M. Saban

Director of Technology

and

Delvis Gonzalez-Lopez

Electrical Engineer

Direct Drive Systems

Cerritos, California

Cassandra Bailey is a Project Engineer, with Direct Drive Systems, in Cerritos, California. She designs high-speed medium-voltage permanent-magnet machines. She began her career as an Integrated Drive Generator Design Engineer with Hamilton Sundstrand, designing an integrated variable speed transmission and AC generator for various military aircraft applications.

Ms. Bailey graduated from Northwestern University with a B.S. degree (Mechanical Engineering, 2003) and is a member of ASME.

Daniel M. Saban is the Director of Technology for Direct Drive Systems, in Cerritos, California. He was previously employed by Hamilton Sundstrand and General Electric. Throughout his 16 year career he has been involved in advanced electromagnetic design of electric machinery including new lamination and winding designs, design tools, and both prototype and product family development for commercial, industrial, and aerospace applications.

Dr. Saban earned a B.S. degree from the University of Illinois - Urbana (Electrical Engineering, 1992), an M.S. degree from Purdue University - West Lafayette (Electrical Engineering, 1993), and a Ph.D. degree from the University of Wisconsin - Madison (Electrical Engineering, 2006), where he specialized in electric motor analysis. Additionally, he holds two M.S. degrees from the University of Wisconsin - Madison (Electrical Engineering, 2002, Mechanical Engineering, 2003) with focuses on power electronics and controls, respectively. Dr. Saban is a senior member of IEEE and a registered Professional Engineer in Indiana and Illinois.

Delvis Gonzalez-Lopez is an Electrical Engineer for Direct Drive Systems, in Cerritos, California. He is an IEEE member and his research interests include design, optimization and control of electrical machines, and primary permanent-magnet machines.

Dr. Gonzalez-Lopez received a B.S. degree from the Central University of Las Villas, Cuba (Electrical Engineering, 1997) and an M.S. degree (Electrical Engineering, 2001). He earned a Ph.D. degree from the University of Concepcion, Chile (Engineering Science/Electrical Engineering, 2006).

ABSTRACT

This paper reexamines some of the usual assumptions in deploying synchronous machines in multi-megawatt, high-speed applications. The detailed design and experimental evaluation of a prototype high-speed, directly-coupled, multi-megawatt permanent-magnet machine that can operate at common gas turbine speeds and power ratings is presented. The maximum, continuous operating speed of the machine being evaluated is 15k rpm to match the shaft speed of compressors and turbines of up to 8 MW in targeted petroleum and chemical industry applications. The machine is characterized by high power-density and high efficiency. The design parameters and the predicted performance are corroborated by component, no-load, loaded and short-circuit tests. The thermal model and the cooling system design are evaluated and calibrated by the temperatures registered during the tests. The total measured losses and the allocation of losses across components are compared with the losses predicted by various analytical and numerical models.

INTRODUCTION

High-speed machines have become an increasingly attractive design solution in applications where it is desirable to eliminate gearboxes and their associated accessory systems. For example, high-speed electric motors with variable-speed drives have been shown to have an advantage over gas turbines as a prime mover for natural-gas compressor applications when both environmental and economic factors are considered (Wood, et al., 1997; LaGrone, et al., 1992). Another advantageous application for high-speed machines is power generation when directly coupled to a gas turbine. High-speed machines can be operated at frequencies an order of magnitude above line frequency, which allows the machines to be smaller than conventional machines in the same power rating, which yields significantly higher power density than with a conventional alternative.

Due to the better power-to-weight ratio, smaller size, and higher efficiency compared to induction machines, high-speed permanent-magnet (PM) machines are a topology being recently considered for subsea, offshore and shipboard applications (Weeber, et al., 1997; Shade, 2008). Both synchronous (PM or

wound-field) and asynchronous (induction) machines have been considered for these applications, however there are significant advantages inherent in a PM machine. Therefore, the differences between these machines warrant further discussion.

The wound-field synchronous machines discussed by LaGrone, et al. (1992), and Gilon (1991) and the squirrel-cage induction machines discussed in Arkkio, et al. (2005), and Evon and Schiferl (2004) were discounted for high speed, multi-megawatt applications because of the complex rotor construction typical to these types of machines. PM synchronous machines and solid rotor induction machines do not suffer from many of the same difficulties (Walter, et al., 2007), as they do not have a field winding or a rotating rectifier and can consequently achieve a higher rotor stiffness with the same rotor outer diameter (OD) and magnetic length. The difference between multi-megawatt high-speed PM machines and their lower powered brethren as studied by Melfi, et al. (2006), and Bianchi, et al. (2004), should also be highlighted.

High-speed PM machines typically have surface-mounted magnets and are sleeved. Many low-power designs can be achieved without a sleeve or with a sleeve of insignificant thickness. A multi-megawatt high-speed PM machine will typically require a sleeve several times larger than the mechanical gap or the order of magnitude of the magnet thickness. Laminated rotor cores and/or embedded magnets considered in some low-power designs do not offer either the radial stiffness or mass containment required for many applications. The sleeve provides the containment and a solid rotor core, or hub, provides stiffness. Common sleeve materials are nonmagnetic high-strength alloys (Weeber, et al., 2007), premolded graphite or carbon composite, and wound-in-place carbon-fiber or carbon-fiber-composite. Of these, the carbon-fiber winding offers the highest strength while providing minimal conduction paths for eddy currents induced by air-gap flux disturbances.

While Arkkio, et al. (2005), were primarily focused on high-speed applications of not more than one or two megawatts, the observation that induction machines will require a larger diameter than an equivalent PM machine should not be lost on the reader. As the power rating becomes higher, the rotor speeds become lower, but the diameters grow. Arkkio, et al. (2005), suggests that the rotor tip speed of 250 m/s to be the upper limit for applying PM machines in favor of solid rotor induction machines. This design value does not directly connect the tip speed to the sleeve stress. Certain design choices, in particular magnet thickness and rotor construction, can influence the sleeve stress dramatically but have no effect on tip speed. For this reason, it is the sleeve stress that determines the limit of rotor containment (and ultimate speed) and the tip speed should only be used as a parametric indicator or rule-of-thumb. Gilon (1991) limits the useful range of wound-field synchronous machines to 8000 rpm but does not tie that to a rotor diameter, or power rating.

Arkkio, et al.'s (2005), assessment that solid rotor induction machines suffer from both poor efficiency and low power factor when compared to PM machines is corroborated by Gilon (1991), who cites the low efficiency of solid rotor induction machines and Walter, et al. (2007), who present performance data for such a machine that shows even at partial load the power factor is quite low (less than 0.7). However, it is not clear how much power factor reduction is due to the selection of the rotor construction and how much is due to the choice of pole count (a two-pole machine versus the four-pole machine presented herein and that of Weeber, et al., 2007). The typical tradeoff between two-pole machines and four-pole machines is between power factor and efficiency, since two-pole machines operate at half the frequency of four-pole machines for the same shaft speed, but tend to have higher aspect-ratio stator slots and longer end turns. In addition, two-pole machines will tend to be physically larger for the same power rating when the rotor diameter is held constant.

The high-speed, sleeved PM machine has an intrinsically larger magnetic air-gap than the unsleeved PM machine due to the sleeve thickness and the increased magnet thickness required to force an equivalent amount of flux through the larger magnetic gap. This larger magnetic gap provides better demagnetization protection, especially under short-circuit conditions.

With the higher power-density and frequency of high-speed machines also comes higher loss-density. Special attention must be paid to the choice of lamination material, coil construction, and cooling system for what would otherwise be a typical stator and housing design. The potential of PM machines to demagnetize under extreme temperature is often used as a factor in dismissing them for applications where robustness is required (Evon and Schiferl, 2004). The choice of samarium cobalt mitigates this risk. In the case of composite sleeve machines, the maximum sleeve operating temperature represents another design constraint that may supersede the magnet material selection. The machine design presented here benefits from a relatively large magnetic gap and near immunity to demagnetization.

This paper presents the design and experimental evaluation of a permanent-magnet machine prototype targeted for 8 MW at 15k rpm. The equivalent circuit parameters obtained from open-circuit (OC), short-circuit (SC) and zero-power factor (ZPF) testing are compared with finite element (FE) results and the results are used to improve the assumptions in the FE model. Short-circuit testing provided the waveform used to predict the transient and subtransient reactance. Stator-only (three-phase inductor) testing provided a means to calibrate the contact resistance used in the thermal model, at thermally stable current loadings not available in other early test configurations. Full-speed testing as a generator with a passive 3 MW load was carried out and the results are compared directly to the developed equivalent circuit and thermal models. Rotordynamic predicted performance is verified by an impact modal test and full speed operation.

DESIGN SPECIFICATION

The petrochemical industry would benefit from a high-speed, medium-voltage PM machine to drive centrifugal compressors or be directly driven by gas turbines. The PM machine has reduced system weight, higher operating efficiency, and a smaller envelope than a conventional solution (Evon and Schiferl, 2004). Directly coupling the motor to the compressor or the generator to the turbine eliminates the need for a gearbox and its inherent maintenance costs and performance penalties. By utilizing magnetic bearings the machine maximizes the benefits of a lube-free system. Magnetic bearings can operate at higher speeds with less loss than certain types of mechanical bearings, which are constrained by size and lubrication type.

Figure 1 shows a selection of gas turbine ratings that are well matched to an eight megawatt product family operating at a rated speed of no more than 15,000 rpm. The triangle shows the target applications for a product family rated at 8 MW and 15,000 rpm maximum (Table 1).

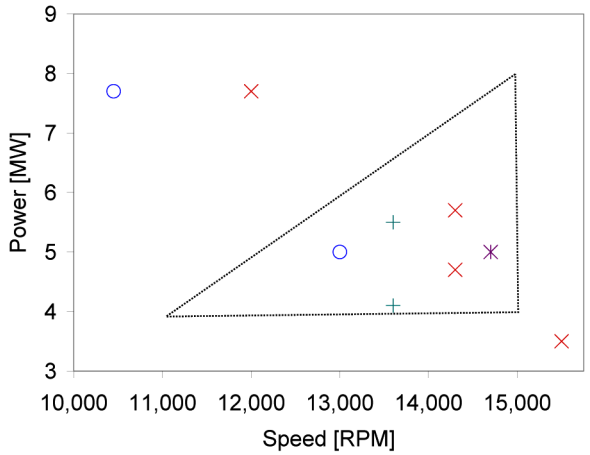

Figure 1. Gas Turbine Ratings from Various Manufacturers. (Courtesy Compressor Tech Two, 2004)

Table 1. Required Specification of a High Speed Medium Voltage Machine.

Item	Specification
Power Rating	8 MW
Rated Speed	15 kRPM
Overspeed	18 kRPM
Drive Rating	6.6 kV, 1 kA
Sleeve Configuration	Wound Carbon Fiber
Cooling Configuration	Water/Glycol Stator Jacket
	Curtain Air Flow over End-Turns
	Stator Mid-Stack Air Flow
Bearing Configuration	2-Radial, 1-Thrust Magnetic Bearing Ball Bearing for Touch Down
	-or-
	2 Duplex Pairs Angular Contact Oil Lubricated Ball Bearings
	-or-
	1- Radial, 1-Combination Radial-Thrust Tilt-Pad Fluid Film Bearings

DESIGN AND ANALYSIS

Electromagnetic Sizing

The electromagnetic sizing of the machine tends to be of secondary importance, behind the mechanical limits of the rotor. The operational speed is driven by market analysis (Figure 1) and a rotor tip speed rule-of-thumb is used as a starting point for the rotor design. The rotor diameter is selected ultimately by iterating between the rotor containment and electromagnetic analyses. The rotordynamic response determines the maximum rotor length, and hence the power limit for the product family. The stator design follows conventional lines, initially using a target current density and finally a detailed thermal analysis based on the electromagnetic loss estimate.

Electromagnetic Losses

Although the stator is very similar in construction to a conventional machine a few loss mechanisms must be specifically addressed. Relatively thin, low loss silicon steel is used to contain losses under the high-frequency operation. Special care must be taken in selecting the strand configuration in the multi-strand, multi-turn form-wound coils to contain strand losses under high-frequency operation. Commercially available lumped-parameter circuit simulators with core loss and copper eddy-loss models were used to predict stator losses. These calculations were compared to results obtained with a commercial electromagnetic finite element analysis (FEA) software and published, closed-form analytical methods.

Rotor losses due to eddy-currents were predicted using a time-stepping, rotating-grid solver from the same commercial FEA software. The solution was obtained with a two-dimensional analysis that ignored the axial segmentation of the magnets and the electrical isolation between each other and the shaft. This approach overstates the losses and they were found to be insignificant when compared to the rotor windage.

Rotor Containment

An FEA tool is used to model the rotor geometry including rotor hub, magnets that are sized by the electromagnetic design, and an initial sleeve design. Hoop stress in the sleeve, von Mises stress in the magnets and sleeve, and contact pressure between the rotor shaft and magnets and between the magnets and sleeve are analyzed at varying speeds and temperatures (Figure 2). Rotor geometry is modified and the analysis iterated until the stresses and pressures fall within design limits.

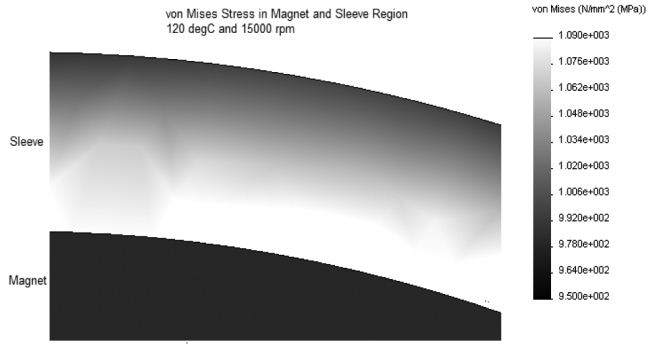

Figure 2. Von Mises Stress Distribution at 15k rpm and 120°C.

The rotor geometry is then set and can be used to determine the rotor-winding process-variables including tape and rotor temperature, tape tow-tension, and number of tape layers.

The rotor-containment model can then be verified by rotor burst-testing. Previous rotor burst-testing results coupled with tensile-strength tests conducted on wound rings of the carbon-fiber-tape determined the material-stress limits and therefore the rotor-containment sleeve-design limits used. Additional burst-testing data is added to the data already collected and increases the statistical accuracy of the design limits. While the rotor tip speed for this design follows the rule-of-thumb of 250 m/s, the maximum allowable sleeve stress is constrained by the limits of the material and is above that chosen by Arkkio, et al. (2005).

Rotordynamics

A commercially available rotordynamics software package is used to determine the mechanical limits of the machine, such as bearing span, by predicting its dynamic behavior. The solution approach of the software is to lump the mass and inertia of a defined area to create the nodes connected by massless beams.

Two separate configurations are discussed: a rotor supported by magnetic bearings and a rotor supported by ball bearings in a resilient mount. The bearings for both configurations are modeled as dynamic supports with variable stiffness and damping.

The magnetic-bearing configuration (Figure 3) consists of two radial-support bearings, one at either end of the shaft and a separate active-thrust bearing at the coupled end to compensate for any axial loading of the coupled system. Touch-down bearings for start-up and shut-down operations are grease-lubricated ceramic-ball bearings. A coupling appropriate to the machine size was chosen and is modeled as a cantilevered weight. Due to the nature of magnetic bearings, the main-housing support-structure does not affect the rotordynamic performance and therefore is not included in the system-level model.

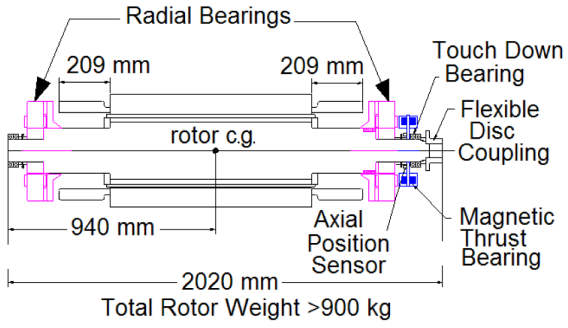

Figure 3. Magnetic Bearing and Rotor Layout.

The ball-bearing configuration consists of oil-lubricated and -cooled angular-contact ceramic-ball bearings that are preloaded in a back-to-back arrangement. The preloaded ball bearings are mounted in an oil squeeze-film damper for load reduction. As with

the magnetic-bearing configuration a coupling half-weight is added to the drive end of the machine as a cantilevered weight. The stiffness and damping of the resilient mount are included in the system-level model; however the frame is considered infinitely stiff and is therefore not included.

The rotor itself is modeled with the solid rotor-hub as the only source of stiffness; the magnets and sleeve are modeled as parasitic weight at the proper diameter. Based on modal impact testing of rotors built previously, it is known that the magnets and sleeve do add some stiffness to the rotor. This stiffness is difficult to predict exactly due to variations in the magnet bonding and sleeve winding process from rotor-to-rotor and is therefore neglected, creating inherent margin in the analysis. This is a very conservative approach and the standard design-practice.

The total rotor-weight for this machine is slightly over 900 kg and the bearing span is approximately 1.6 m. The machine with either bearing configuration is designed to run subcritical, or below the first forward bending mode. The PM machine's solid rotor-shaft construction is what allows the machine to run at such high speeds and maintain subcritical operation. This is in contrast to a traditional wound-field synchronous-machine or a squirrel-cage induction machine. Additional design margin can be obtained by limiting the bearing span and maintaining the rotor hub OD as large as possible in the stator end-turn region. The magnetic bearing configuration resulted in a first forward-bending mode of 22,391 cycles per minute (cpm) (Figure 4).

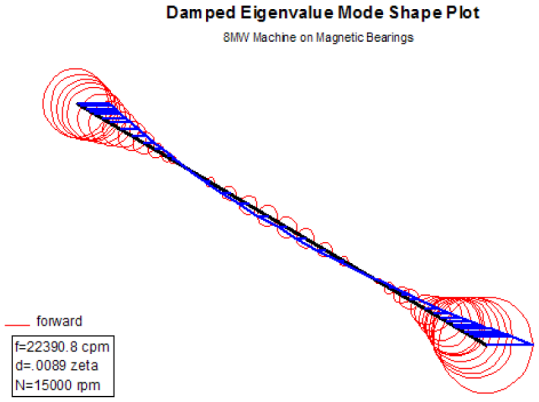

Figure 4. Mode Shape for the First Forward Bending Mode of Magnetic Bearing Configuration.

The ball-bearing configuration resulted in a first forward-bending mode of 21,768 cpm (Figure 5). Both configurations are viable since the first forward-bending mode falls more than 20 percent above the overspeed of the machine.

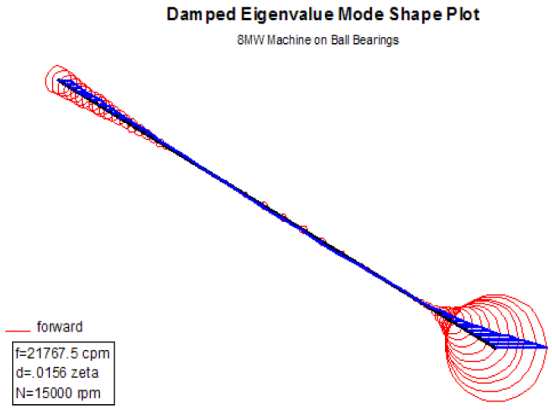

Figure 5. Mode Shape for the First Forward Bending Mode of Ball Bearing Configuration.

The magnetic-bearing control-circuit design depends heavily on the expected system load response at the location of the support-bearing actuators. The bearing load-response plots are also important to the ball-bearing configuration since this indicates the vibration that will be seen during operation. The response plots shown, magnetic-bearing configuration (Figure 6) and ball-bearing configuration (Figure 7), are based on four times the maximum allowable imbalance per ISO 1940/1-1986 machine category G2,5 in phase with each other with a two plane balancing scheme. There are no major gyroscopic effects for either configuration and therefore the horizontal and vertical responses are identical, only the horizontal responses are shown for clarity.

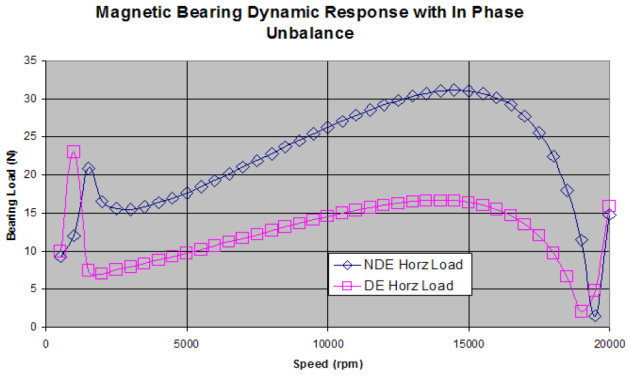

Figure 6. Bearing Load Response Plot for Magnetic Bearing Configuration.

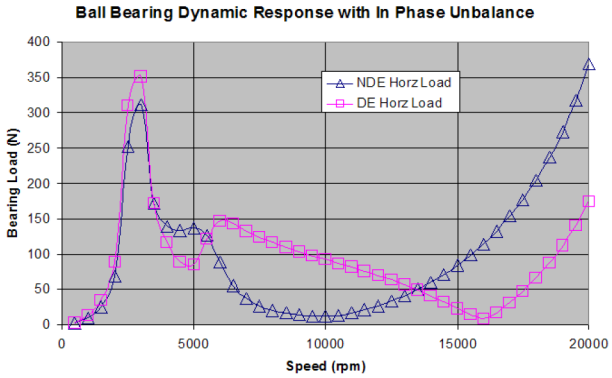

Figure 7. Bearing Load Response Plot for Ball Bearing Configuration.

Cooling

A lumped-parameter model is used to model the machine geometry including rotor, stator, and cooling jacket to prescreen cooling system topologies. Finally a computational-fluid-dynamic (CFD) model of the system was used to determine the machine operating point. A maximum design temperature limit for coil insulation and carbon fiber analysis was set at 150°C.

A separate aluminum cooling jacket with a press fit to the stator back-iron extracts heat through a water/glycol cooling flow. The interference fit is selected for structural integrity as well as to reduce the insulating effects of a microscopic air gap, or contact resistance, between the cooling jacket and the stator back iron.

Curtain-air flow removes heat out of the end turns without being choke-limited by the radial air-gap size. Although the wound-carbon-fiber sleeve acts as a thermal insulator, cooling flow through the radial air-gap provides some cooling to the rotor as well as cooling the stator tooth tips, therefore cooling air flow is actively blown through a mid-stator-stack vent and into the radial air-gap and out over the stator end-turns (Figure 8). Loss input is determined and allocated from the electromagnetic analysis tools discussed previously.

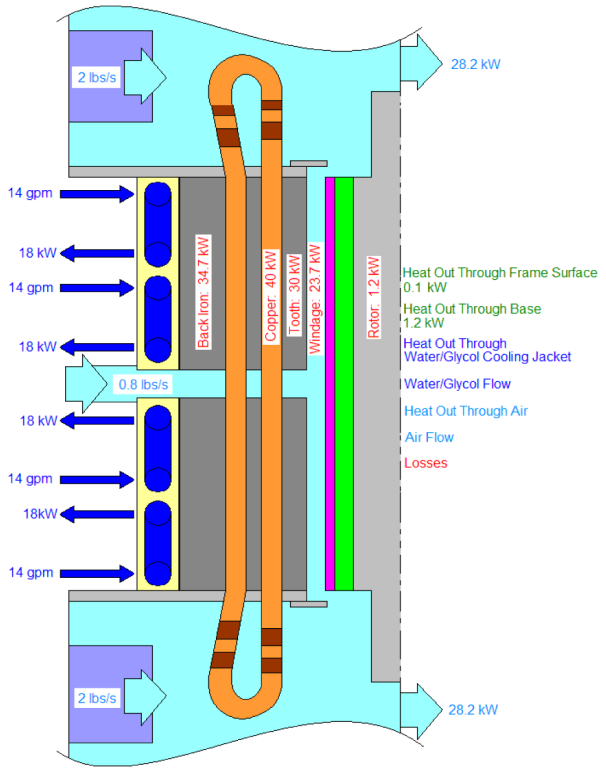

Figure 8. Machine Cross-Section Showing Cooling System.

The CFD analysis tool utilizes the actual 3-D solid-assembly model. Losses are represented as heat flux on the surface of the appropriate component, for example windage losses are modeled as heat flux on the surface of the rotor-containment sleeve. Cooling-flow inlets and outlets are defined; however the actual path and velocity of the flows were calculated by the CFD model (Figure 9). The conclusions of the lumped-parameter model were confirmed and refined by the CFD analysis.

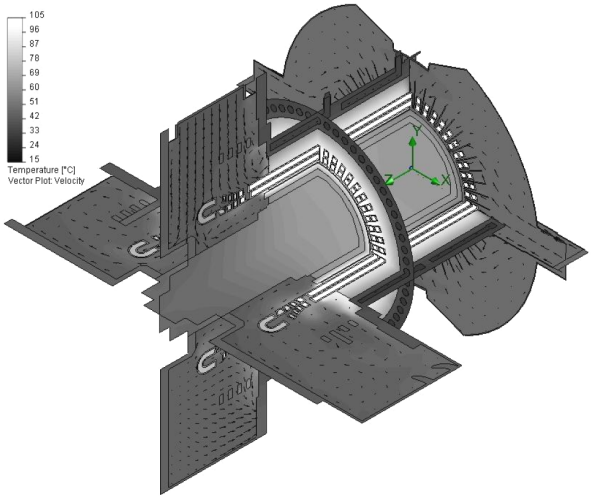

Figure 9. Solid Model Results from Computational Fluid Dynamic Analysis of Machine.

TESTS AND RESULTS

Equivalent Circuit Model

Nelson, et al. (2006), presented the details of the two-megawatt high-speed alternator (HSA), which was used to validate the electromagnetic analysis tools prior to the prototype-machine build. The higher-than-predicted rotor-field strength reported by Nelson, et al. (2006), was taken into account when designing the eight-megawatt machine by adjusting the magnet material-properties, both in the drawing tolerance and in the electromagnetic model. Electromagnetic aspects of the stator design are similar-to or no-different-from a conventional machine and so model validation of stator quantities is of lesser concern and is not presented here.

A standard exists (IEEE 115, 1995) for testing synchronous machines, however many of the tests assume an adjustable field as with a wound-field synchronous machine. Tests for a PM synchronous machine can be adapted directly where a constant field is allowed. In particular the no-load loss test, the short-circuit test, and open-circuit voltage tests can be preformed. Fortunately this is enough for a simple equivalent circuit model. For PM machines the separate-drive method can be used to obtain the open circuit voltage (V_{OC}) and no-load losses from no-load generator mode. The retardation method is used for total no-load losses.

An open-circuit generator test was carried out and terminal voltage of the prototype was recorded at several speeds. With PM machines the excitation flux cannot be removed and therefore the friction and windage loss cannot be separated from iron loss and copper eddy loss. The total no-load losses were obtained, as is explained below, from spin-down operation.

The sudden short-circuit test presented in (Arkkio, et al., 2005) was used to obtain the transient and subtransient parameters from the current waveforms and the open-circuit voltage immediately before the sudden short circuit.

The equivalent circuit parameters were calculated from these test results and are shown in Figure 10. The synchronous inductance (L_S) was calculated for several speeds and similar values were obtained, as expected. For the rated speed (15k rpm with a frequency, f, of 500 Hz) X_S is 2.2 Ω, calculated from Equation (1).

$$X_s = 2\pi \cdot f \cdot L_s \tag{1}$$

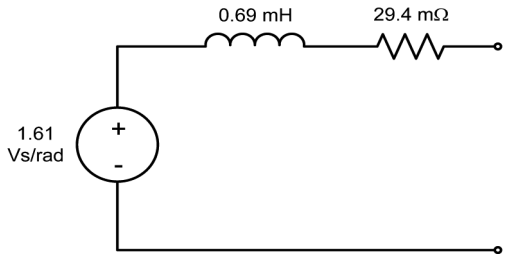

Figure 10. Simple Voltage-Driven per Phase Equivalent Circuit.

The open-circuit voltage is expressed as the speed dependant voltage source of Figure 1. The open-circuit voltage constant, K_V (1.61) must be multiplied by the rotational speed in radians per second to arrive at the per-phase open circuit voltage.

Although the voltage-driven equivalent-circuit model is commonly used, a current source model can also be used (Sebastian, et al., 1986). The parameters of such model were calculated for the presented machine and are shown in Figure 11. The synchronous inductance is separated into the magnetizing and leakage components. The magnet is represented as a current source as is more common in electromagnetic field analysis.

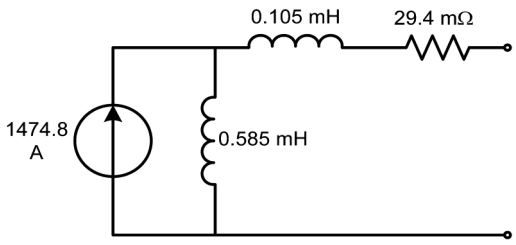

Figure 11. Simple Current-Driven per Phase Equivalent Circuit.

Both equivalent circuit models are most valid at or near the frequency and current that the tests were performed at. The parameters can vary with saturation, temperature and frequency, and these effects are typically included in a more detailed model. In general, more detailed models are used to predict machine parameters prior to build and test. These models can be lumped parameter (LP) models, finite element models or some hybridization of the two.

A two-dimensional (2D) FE analysis (transient with motion) was carried out to predict the open circuit voltage before machine build, and then again after test with the magnet strength adjusted to match the test. This parameter is very sensitive to the magnet material properties that vary with temperature and are not precisely well known prior to fabrication even by the manufacturer. Table 2 compares the FE results with the measured line-to-line voltage. The first row shows the predicted induced voltage from initial FE analysis using magnet material data supplied by the manufacturer. The second row contains the value of V_{OC} from an FE model with the magnet strength corrected from tests results. The values presented are for 15k rpm; however open-circuit voltage varies linearly with speed with close correlation.

Table 2. Open-Circuit Voltage at 15k rpm.

	V_{OC} [V]
Initial FE prediction, 20°C	4685
Corrected FE results, 20°C	4392
Measured	4378

However for direct measurement, the line-to-line voltage scaled by the speed in rotations per minute is more convenient because of this linearity. The open-circuit voltage, V_{OC} was measured for a complete speed range from no-load generator tests and normalized for speed, as depicted in Figure 12.

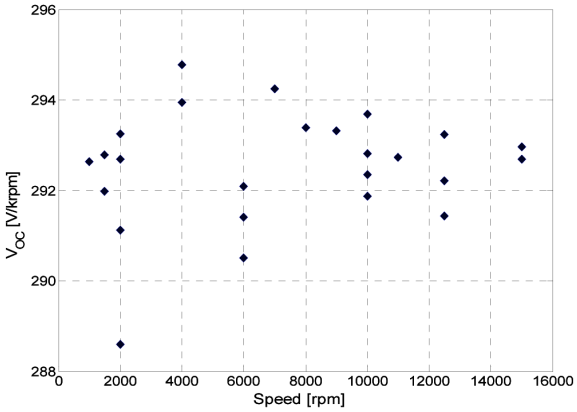

Figure 12. Measured Open Circuit Voltage.

Short Circuit Transient Response

Several sudden-short-circuit faults were imposed across the machine terminals, with the machine operating as a generator at low speed (2k rpm). A typical, measured current characteristic is shown in Figure 13.

During the short-circuit tests the stator current is only limited by the stator impedance; a high armature-reaction flux is imposed in the axis aligned with the highest flux density of the rotor magnets (the direct, or d-axis). In a poorly designed machine this condition can cause an irreversible degradation of the magnetic properties (Rosu, et al., 1999). Therefore, it is important that the machine will avoid demagnetization during the short circuit condition.

Table 3 shows the average open-circuit voltage measured before and after short-circuit testing. The total operation time under short-circuit condition was three hours and ten minutes. During this test three-phase short-circuits were imposed 13 times at the machine terminals. No observable demagnetization has occurred. The large magnetic gap (i.e., the mechanical air gap + sleeve + magnet) imposes a high reluctance path to the armature-reaction flux and reduces the risk of demagnetization. The samarium cobalt magnets are chosen specifically for their high temperature operation and resiliency to demagnetization. These two factors contributed to the resiliency under the fault condition.

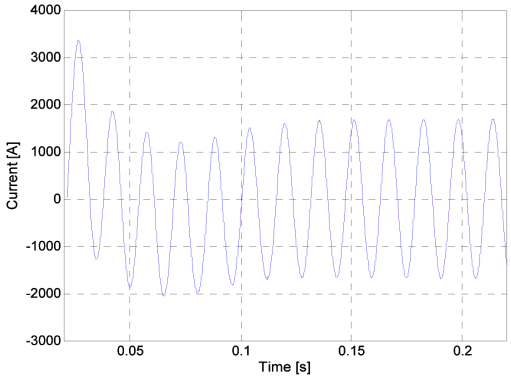

Figure 13. Measured Short Circuit Current.

Table 3. Normalized Average Open-Circuit Voltage Constant Measured before and after Short Circuit Tests.

	Before SC Test	After SC Test
V_{OC} [V/kRPM]	292.93	292.19

The total flux is reduced in a short-circuit test because the stator current produces a demagnetizing flux that directly opposes the rotor excitation. Therefore, a low saturation condition is present in the magnetic circuit. The calculated value of the steady-state unsaturated reactance (X_{us}) is compared with FE results in Table 4.

Table 4. Unsaturated Reactance (Xus).

Speed [RPM]	X_{us} [Ω]	L_{us} [mH]
At 2000 (FE)	0.272	0.650
At 2000 (SC Test)	0.276	0.660
At 3000 (FE)	0.408	0.649
At 3000 (SC Test)	0.415	0.660
At 15000 (FE)	2.06	0.656

Table 5 shows the transient (L_d') and subtransient (Ld") inductances obtained from the short-circuit test and the calculated equivalent inductance at 15k rpm. There is negligible difference in these quantities due to rotational speed, supporting key assumptions regarding linearity with respect to frequency (especially for these unsaturated quantities), as with the open-circuit voltage. The transient (X_d') and subtransient (X_d") reactance per unit of the machine base impedance are presented in Table 6.

Table 5. Transient and Subtransient Reactance.

	L [mH] at 2.0 kRPM	L [mH] at 15.0 kRPM
Transient	0.525	0.525
Sub-transient	0.453	0.452

Table 6. As Tested Parameters in per Unit, Xd' and Xd".

	Prototype
X_d' [pu]	0.525
X_d" [pu]	0.453

Thermal Model and Stator-Only Test

The machines discussed by Nelson, et al., (2006) were used as part of the thermal-model verification. Two HSA machines were coupled together in a back-to-back configuration with one operating as a motor driving the other (as a generator) for testing purposes. In this configuration the cooling system was adjustable and thoroughly instrumented. The HSA machines were run with different cooling and load combinations per Table 7. Both the lumped parameter and FD models were refined based on these tests until they reasonably matched the test data (Figure 14). In this way the lumped-parameter and CFD models were verified. The lessons learned from the HSA testing and modeling such as the significance of the heat lost to the ambient air and through the machine feet were incorporated into the eight-megawatt cooling system design.

Table 7. Test Configuration for Cooling Model Validation.

Test Set-up	Load [kW]	Liquid Cooling	Air Cooling
1	450	Yes	Yes
2	No Load	Yes	Yes
3	No Load	Yes	No
4	No Load	No	Yes

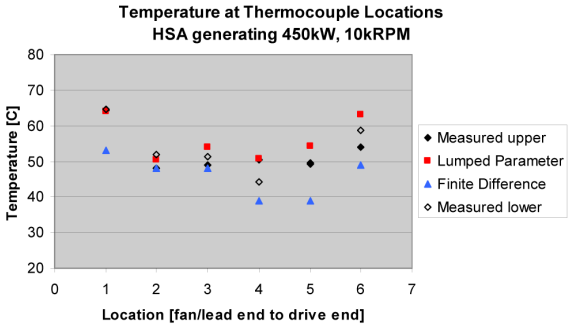

Figure 14 Comparison Plot of Analytical Prediction and Test Data.

As depicted in Figure 8 the heat generated in the machine during operation is removed by a two-part cooling system; liquid cooling provides cold flow through the stator outer-diameter cooling-jackets and forced air cools the air gap and end-turns of the stator winding. In normal operation, a blower pumps air to the mid-stack of the stator, where it splits and flows toward the ends through the air gap. A second blower forces the air over the stator winding end-turns. This was the cooling arrangement selected for this prototype unit and may not be indicative of a production machine.

The heat transfer in typical electrical machines is by conduction, convection and radiation. The relatively small temperature difference between solid components of the prototype allows radiation to be neglected in the theoretical analysis. The heat transfer coefficient of the end-turns and the contact resistance between stator core and cooling jacket significantly influence the cooling system effectiveness, but are difficult to determine analytically.

Prior to the complete build of the prototype machine, a "stator-only" test used ambient air flow and the water cooling system to choose a stator contact resistance for the thermal model. Current magnitudes of varying frequency and magnitude were injected into the stator winding. Stable temperatures were measured with thermocouples installed on the surfaces of the end-turns and resistance temperature detectors (RTDs) in the stator slots. Measured temperatures were corrected for the temperature gradient across the insulation for comparison with the predicted copper temperature.

A CFD model was used to validate the thermal model for a simulated operating condition. The model segregated the stator iron and copper losses. Figure 15 shows the temperature distribution obtained from CFD analysis.

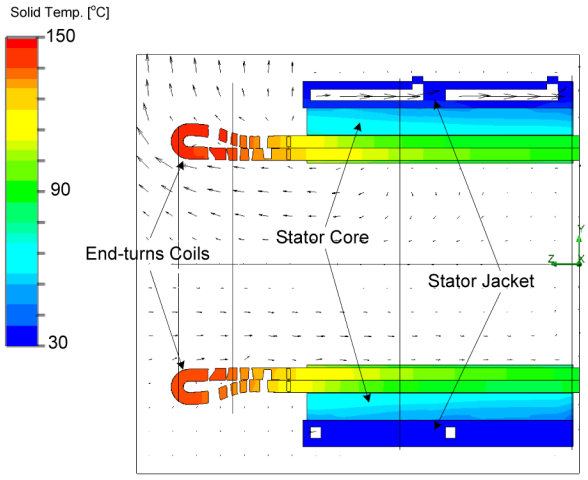

Figure 15. Stator Temperature Distribution (Longitudinal View).

The maximum stator temperature occurs in the coil end-turns, which are primarily cooled by natural convection in this test. The coil slot sections are cooled mainly by conduction to the cooling jacket through the stator laminations. Table 8 shows the calculated and measured stator coil temperatures.

Table 8. Calculated and Measured Stator Coil Temperatures.

	End-turns	Inside the slot
CFD Analysis	140.0 °C	105.1 °C
Measured	137.0 °C	105.0 °C

The total losses are obtained by calculating the input power from the voltage and current measurements. The copper conductors produce ohmic loss from the net current at the operating frequency and eddy-current loss due to the changing magnetic field impressed upon them. There is an additional loss component from the proximity of the conductor strands. Rather than build a strand-by-strand FE model of the stator winding to predict the iron loss, a simple coil model (Figure 16) was used for iron loss calculation for this condition. The copper loss is the difference between the iron loss and the measured input power. Since the prototype was tested in this configuration without the rotor, effectively as a three-phase inductor, the input power is identically the output power. The power source in this test was the same power electronic drive used in later testing.

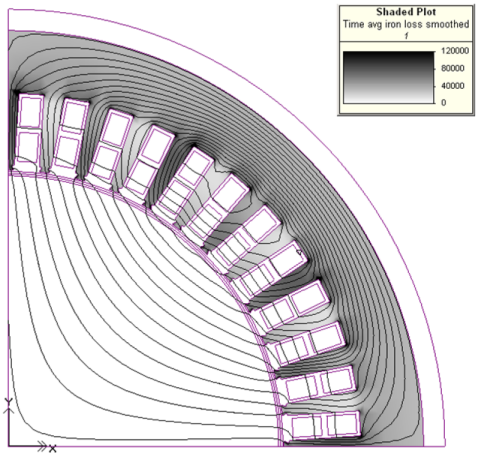

Figure 16. Iron Loss Distribution in the Stator from FEA during Stator-Only Testing.

The total measured loss in the CFD model was used to find the loss distribution that produces the temperature profile observed during the test. The iron loss is taken from the FE model shown in Figure 6 and distributed in the stator core. The copper loss is split between the portion of copper in the slots and the end-turn winding. The heat transfer coefficients and contact resistance used in the thermal model are adjusted empirically (within heuristic bounds) to obtain a final thermal model and loss distribution. A heat balance using the measured flow and temperature of the cooling liquid and the predicted heat removal via convection agreed with the total loss measured at the stator terminals. Table 9 presents the loss allocation from the thermal model for this test condition.

Table 9. Loss Segregation for Stator-Only Test.

	Iron Loss [kW]	Slot Cu Loss [kW]	End-turn Cu Loss [kW]	Total losses [kW]
CFD Model	10.52	8.28	3.72	22.52

Limitations of the drive used during this testing prevented exploring the entire frequency and excitation range. The flux distribution in the stator under this condition is not the same as that seen under normal operation. The flux distribution and limited frequency and excitation range are not as significant as the fact that the total losses and stator temperatures are lower than expected in operation. A greater temperature rise above ambient would have provided better correlation for the thermal model.

No-Load Losses

The prototype was driven by a PM motor (rated for 22k rpm and 2 MW) during the no-load tests. The 2 MW motor was also run at no-load uncoupled from the prototype and total input power over the speed range was taken to be the no-load losses. The no-load losses of the driven 8 MW machine are calculated by subtracting the loss of the uncoupled 2 MW machine from the no-load loss measured during spin-down of the coupled machines. The power-electronic drive was open-circuited while running the machines at 15k rpm. The speed versus time during coast-down was used to calculate the energy stored in the system. Since the inertia of both machines is known, the kinetic energy can be calculated by Equation (2):

$$E = \frac{(I_M + I_P)\cdot \omega^2}{2} \text{ [J]} \qquad (2)$$

where I_M and I_P are the inertias of the 2 MW motor and the 8 MW prototype respectively and ω is the angular speed in rad/sec. The total power dissipated by the system is given by the decrease in kinetic energy with time. The no-load losses of the prototype were obtained as the difference between both running conditions.

The no-load loss segregation is a challenge in PM machines. The first step is to define the power allocation for open-circuit operation. The no-load losses are composed of total air gap loss due to the friction and windage, mechanical losses in bearings, and magnetic losses in the stator laminations and stator windings. Additionally second-order eddy-current losses may be present in components of the housing and bearing structure. Rotor eddy current losses for this mode of operation are calculated analytically and are found to be negligible. Figure 17 depicts the no-load loss segregation up to 15k rpm.

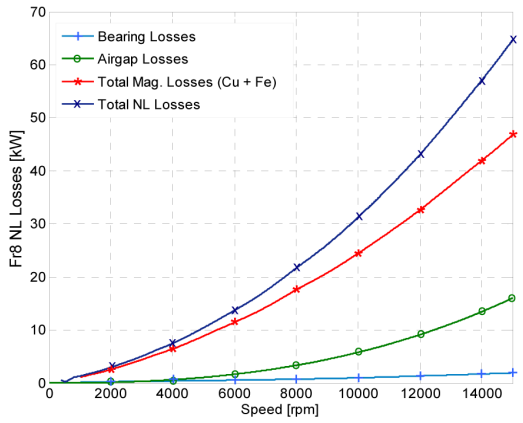

Figure 17. No-Load Loss Segregation.

The air-gap windage loss was calculated analytically for the complete speed range using the air gap dimensions and the temperature recorded during no-load tests. The measurement of the supply and outlet temperatures and mass-flow rate of the coolant were used to calculate the losses in the bearings. The difference between total no-load losses and air-gap and bearing losses are the total magnetic losses (iron loss and eddy-current losses in the stator coils). This analysis was the starting point to distribute the losses in the thermal model to produce the same temperature profile recorded on the open-circuit test.

The rotary excitation flux causes a significant loss in the stator coils due to the eddy-current effect. This loss component is directly dependent on the number of strands size and configuration. A multi-strand FE model was developed to estimate the eddy current losses at several frequencies. Figure 18 shows the current density distribution for no-load generator at 15k rpm using the multi-strand FE model. Since the terminals are open-circuited, the current distribution is due solely to the eddy current from the rotating excitation flux.

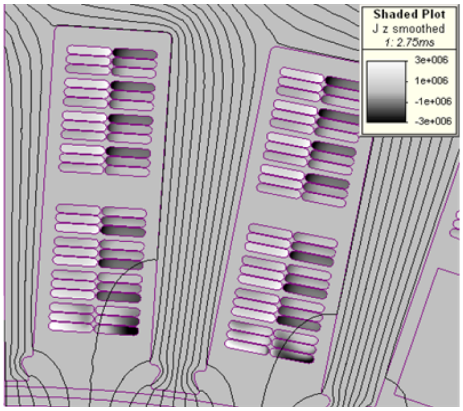

Figure 18. Current Density Distribution in the Stator Coils for the No-Load Generator Case at 500 Hz, 15k rpm.

A number of analytical methods for the eddy current losses in the stator coils (Say, 1976; Walker, 1996; Shanks, 1976; Fink and Beaty, 2007) were evaluated. The copper losses obtained from the FE model are compared in Table 10 with thermal model and analytical results.

Table 10. Eddy Current Loss in Stator Coils.

f [Hz]	FE	CFD	Say [14]	Walker [15]	Shanks [16]	Fink [17]
100	0.32	1.58	18.13	0.08	0.22	4.08
300	2.39	7.47	23.96	0.72	1.99	36.74
400	3.99	11.71	29.07	1.23	3.53	65.34
500	5.91	16.80	35.63	1.98	5.52	102.05

Of the analytical eddy current calculation methods, only Shanks (1976) gives a result close to the FE model. This was the only analytical method calibrated with test data. All other methods were derived from first principles alone. The FE model used was strictly 2D and so only the portion of the winding in the slot was considered, although the strand placement and interconnection were faithful to the machine, as built. None of the methods approached the CFD model results.

A commercial LP model was also used to predict the no-load loss, as well as for various other load conditions. This model had been calibrated with some initial test data from other machines, but it assumes a uniform current distribution in the windings—in this case, zero current. The iron losses used in the LP model make use of the Steinmetz (1984) coefficients interpreted from manufacturer supplied data (Miller and McGilp, 2004). Table 11 compares the total machine loss distribution for the no-load condition obtained from CFD, FE and LP models.

Table 11. No-Load Loss Segregation at 15k rpm, 500 Hz.

[kW]	Iron Loss	Slot Cu Loss	Windage	Total losses
CFD Model	29.9	16.8	16.3	63.0
FE Model	20.7	5.9	n/a	n/a
LP Model	24.9	0	20.0	44.9

The winding loss calculation for the LP model does not include the proximity, skin and eddy-current effects. This loss component is zero for open circuit case because it is produced only by the Joule effect ($I^2 \bullet R$). The windage loss in both models can be refined as they should be made to agree much more closely: the LP model used an assumed gap air temperature whereas the gap air in the CFD model agreed with test data. The iron loss allocation is within 20 percent among the three models. Although not desirable, this discrepancy is much less than the copper eddy losses (among these three models and the analytical methods). There can be some confounding between the iron loss and the windage losses since the highest loss density for the iron loss is at the stator tooth-tips, which is in close contact with the air-gap, where the windage is produced. Some of the windage loss is carried away via the tooth tips into the cooling jacket, so it is not surprising that the sum of windage and iron losses are very close between the CFD and LP models. The iron losses as calculated by the FE model are a function of the numerical calculation procedure, the details of the model and material properties. The FE and LP models should be in closer agreement in general, however the LP model assumes a particular flux distribution along predetermined paths whereas the FE model calculates the expected flux distribution from the machine geometry and excitation in total. It is likely that the LP model uses slightly more pessimistic assumptions, but that both LP and FE models are using an optimistic representation of the material properties.

Rotordynamics

The initial design of the machine included magnetic bearings for both radial and axial support, however the prototype machine under discussion was designed and built on angular contact ceramic ball bearings mounted in a preloaded back-to-back configuration in an oil squeeze film damper. Therefore the total system model includes the rotor, angular contact ball bearings, and oil squeeze-film dampers. The frame of the machine is considered infinitely rigid and is therefore not included in the analysis. The commercially available software described earlier was used to predict the systems' natural frequencies, both free-free and damped with corresponding mode shapes, and the dynamic response based on predicted imbalance.

The program lumps the mass and inertia of a defined area and creates nodes connected by massless beams. The rotor itself is modeled conservatively; the magnets and carbon fiber sleeve are modeled as a mass at the appropriate distance from the center of the shaft, however they are assumed to contribute no structural stiffness to the rotor. This conservative approach results in predicted natural frequencies that are lower than the actual, but this analysis method is still utilized to compensate for manufacturing variation. Previous experience also validates the approach that the segmented magnets and carbon sleeve do not contribute appreciably to the overall rotor stiffness.

In order to validate the rotordynamic model the rotor was hung vertically and subjected to a modal impact (Figure 19). Again the predicted natural frequencies should be lower than the measured natural frequencies due to the conservative nature of the analysis.

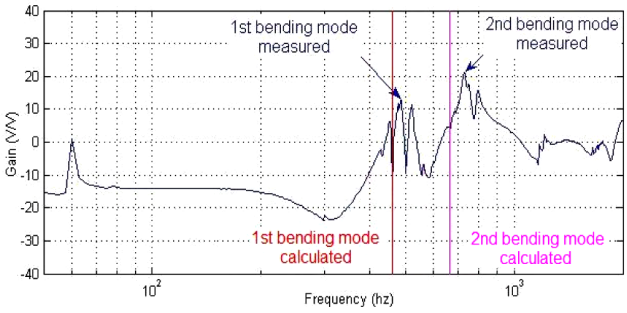

Figure 19. Rotor Impact Modal Test Results.

The dynamic behavior of the rotor was continually monitored during testing at the outboard side of each bearing support on both the drive end and nondrive end of the machine. Three one-axis accelerometers were oriented vertically, horizontally, and axially at both ends for a total of six accelerometers. Proximity probes were oriented vertically and horizontally at both ends and additionally one probe was mounted axially at the nondrive end for rotor growth and total axial displacement monitoring. The proximity probe data were used to plot the rotor orbits. The predicted peak-to-peak displacement at either end was 0.00127 cm (0.5 mils) to 0.01143 cm (4.5 mils) when going through the rigid body modes and approximately .00254 cm (1.0 mils) at 15k rpm, depending on the exact distribution of rotor imbalance. The observed displacement of the shaft during operation fell well within the predicted range (Figures 20 and 21) at rotor thermal steady-state. Prior to thermal steady-state of the rotor vibration and displacement values measured were higher than at thermal steady-state; however they stayed below the maximum predicted levels.

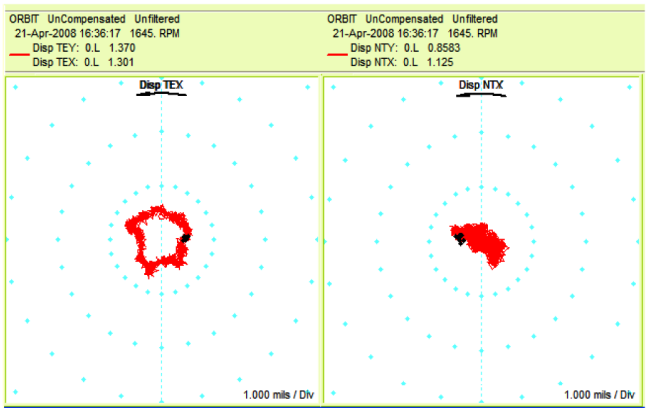

Figure 20. Drive End (left) and Nondrive End (right) X-Y Orbit Plot at 1645 rpm.

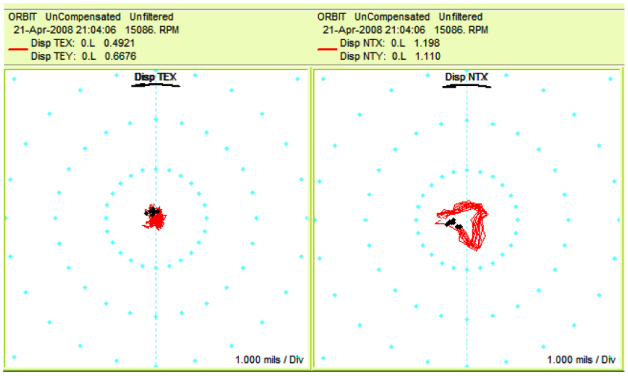

Figure 21. Drive End (left) and Nondrive End (right) X-Y Orbit Plot at 15,086 rpm.

Peak vibration measured at the nondrive end during operation prior to thermal steady-state of the rotor was less than 2 g (rms) at 15k rpm. The vibration at the drive end in all three orientations was less than 1.4 g (rms) at 15k rpm (Figure 22). The dynamic behavior of the system was stable and acceptable for continued operation. Overall the rotor and bearing support system behaved close to predicted levels, confirming that the analysis method was appropriate for the design.

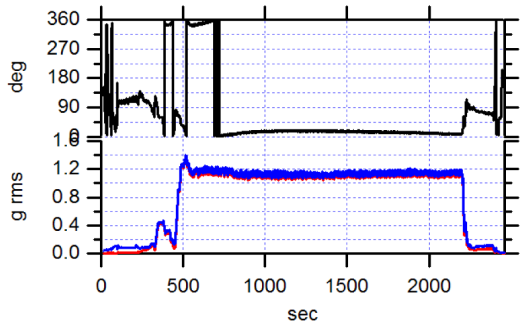

Figure 22. Drive End Vibration Bode Plot for a 40 Minute Test with a Max Rotor Speed of 15k rpm from 500 Sec to 2200 Sec.

3 MW TESTING

Partial load tests were conducted using a resistive load bank and a gas turbine rated for 3 MW at 15k rpm to drive the prototype machine as a generator. Although the turbine is limited to continued operation under load to speed very close to 15k rpm, the resistive load bank can apply the load in steps as small as 125 kW. The load was increased stepwise from 125 kW up to 3 MW, providing several different operating points to compare to the equivalent circuit predictions.

Figure 23 depicts the measured and predicted output power from the equivalent circuit parameters and the LP model. The close agreement between both data sets validates the equivalent circuit shown in Figure 10. The LP model "passive load" case assumes a unity power factor, purely resistive load. The "active load" case assumes that the load power factor is adjusted such that the machine operates with the maximum power conversion.

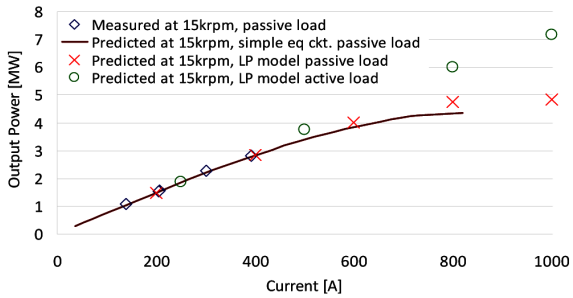

Figure 23. Predicted and Measured Output Power at 15k rpm.

The simple equivalent circuit model uses a resistor in series with the output of the machine that includes the iron and copper loss and agrees more closely with the test data (and CFD) than the LP model. The iron-loss resistor would be better represented as a parallel resistor separate from the winding resistance. This improvement to the equivalent circuit model should provide better agreement with the LP model, at the cost of model simplicity. Retaining the level of model simplicity in Figures 10 and 11 would require a different resistance for each frequency and excitation of interest (and a different inductance as well), which is useful for hand calculations around a well-known operating point, but is exactly the reason why more rigorous LP models are employed for electric machine analysis.

The measured current in steady-state at 15k rpm was 393 A and fed an electric load of slightly less than 3 MW. The analyses below are focused on that operation point. The FE model developed for calculation of the copper eddy-current losses for the no-load condition was excited to correspond with the 3 MW test. The resulting current density distribution is presented in Figure 24.

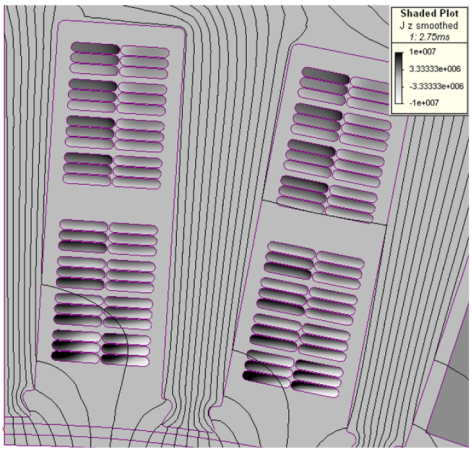

Figure 24. Current Density Distribution in the Stator Coils for the 3 MW Load Generator Case at 500 Hz, 15k rpm.

Table 12 compiles the loss predictions for the FE, LP and CFD models. The FE method has been accepted as a viable means to predict eddy-current effects in rotating machines. The focus of research in this area has been to improve the details of the numerical formulation and computational efficiency of the problem, and not whether or not this is a viable approach (Chari and Csendes, 1977, 1982; Szücs and Arkkio, 1999). So it is surprising that the FE model predicts a significantly lower eddy-current loss than the CFD model supported with test data. It is noteworthy that the difference between the CFD and FE prediction of copper eddy-current loss is maintained between the no-load (Table 10) and 3 MW cases—this gives some insight into the problem. The effect of current loading appears to have been handled consistently between the two models, but resolving the discrepancy lies with understanding the no-load case. This suggests that if no-load testing is used as a baseline for loss allocation, then the effects of loading can be determined numerically (with the FE model).

Table 12. Loss Segregation for 3 MW, 15k rpm Operation.

	Iron Loss [kW]	Slot Cu Loss [kW]	End-turn Cu Loss [kW]	Windage [kW]	Total loss [kW]
CFD Model	33.60	21.2	1.77	17.80	74.37
FE Model	23.77	9.95	1.72	n/a	n/a
LP	24.46	1.91	1.71	20.0	48.08

The FE model and LP model agree better under load than under the no-load case. This is not surprising as the assumptions built into the LP model are expected to be skewed toward "normal" or loaded operation, as this is the condition typically of the most interest. The significant difference between the FE model and LP models (using similar material properties) and the CFD model suggests that the stator lamination material has more loss than the material properties used in the FE and LP models would indicate.

The (2D) FE model losses allocated to the end-turns are derived from the LP model, which does not consider skin effect. It could be conjectured that the total loss budget in the CFD model is misappropriated in this regard, were it not for the close correlation between measured and predicted temperatures (Table 8).

The allocation of losses is more important to the temperature rise prediction of specific components rather than to the power conversion calculation. The discrepancy in losses between the FE and CFD models account for about 0.7 percent change in machine efficiency at 3 MW and less than 0.2 percent change in machine efficiency at 8 MW. However a change of a few kilowatts of loss in a given component is enough to raise the predicted temperatures a non-negligible amount.

CONCLUSIONS

This paper presents a viable medium-voltage, high-speed PM machine design well suited for replacement of, or coupling with, a variety of gas turbines. The machine's stator consists of thin, low-loss silicon-steel laminations and multi-strand, multi-turn form-wound coils and was designed for high frequency operation using a commercially available FEA program. The machine will be supported by either one thrust and two radial magnetic-bearings with ball bearings used as touch-down bearings during start-up and shut-down two duplex-pairs of oil-lubricated angular-contact bearings or one radial and one combination radial and thrust tilt-pad fluid-film bearings.

The rotordynamic analysis completed shows the machine to be running subcritical with a first forward bending mode 20 percent above the overspeed condition and over 20 percent above the nominal operating speed for both configurations. The response plots show acceptable bearing loads based on the bearing support structures for each configuration. Testing of the machine verified the analytical tool given the conservative assumptions used. Therefore the method used can be applied to similar machines without relying on machine or component level testing for needed accuracy.

Cooling for the machine consists of cooling air entering through a mid-stator vent as well as independent cooling flows over each of the end-turn sections and a water/glycol cooling flow through a pressed-on cooling jacket on the stator outer diameter. By independently blowing cooling air over the end turns the total flow-rate is not restricted to the rotor air-gap choke flow and can be significantly increased to meet the thermal requirements of the machine.

The thermal model utilizing computational fluid dynamics was able to provide insight into the loss distribution within the machine when correlated with component test data. This physics-based model can be extended for machines of similar construction without loss of generality.

Analytical and numerical methods based on electromagnetic models, both lumped parameter and finite element proved to be inadequate for *a priori* loss prediction, especially at no-load. This is an area to be explored in greater detail since there are many factors that influence these predictions and not all loss mechanisms or all components of the electric machine were considered.

A combination of LP and FE methods can be used for reliable power conversion calculations. However, the simplest equivalent circuit models should be eschewed at higher excitation levels.

A loss budget above the initially predicted values should be maintained for prototypes developed without the benefit of similar machines to calibrate the analysis and design tools. The cooling system used for machine development can be oversized to compensate for discrepancies between initially predicted and as-built machine losses.

REFERENCES

Arkkio, A., Jokinen, T., and Lantto, E., 2005, "Induction and Permanent-magnet Synchronous Machines for High-speed Applications," Proceedings Eighth International Conference on Electrical Machines and Systems ICEMS 2005, *2*, pp. 871-876.

Bianchi, N., Bolognani, S., and Luise, F., 2004, "Potentials and Limits of High-speed PM Motors," *40*, (6), pp. 1570-1578.

Chari M. V. K. and Csendes, Z. J., 1982, "New Finite Element Techniques for Skin Effect Problems," IEEE Transactions on Magnetics, *MAG-18*, (2).

Chari M. V. K. and Csendes, Z. J., 1977, "Finite Element Analysis of the Skin Effect in Current Carrying Conductors," IEEE Transactions on Magnetics, *MAG-13*, (5).

Compressor Tech Two, 2004, "2004 Basic Specifications—Mechanical Drive Gas Turbine Engines," pp. 115-117.

Evon S. and Schiferl, R., 2004, "Direct Drive Induction Motors," Conference Record of the 2004 Annual Pulp and Paper Industry Technical Conference, pp. 49-54.

Fink D. G. and Beaty, W. H., 2007, *Standard Handbook of Electrical Engineering*, Fifteenth Edition, McGraw-Hill.

Gilon, D. C., 1991, "Design and Tests of a 6 MW, 10000 Rpm Induction Motor," Proceedings Fifth International Conference on Electrical Machines and Drives, Publication No. 341, pp. 6-10.

IEEE 115, 1995, IEEE Guide: Test Procedures for Synchronous Machines.

LaGrone, S. C., Griggs, M. C., and Bressani, M., 1992, "Application of a 5500 Rpm High Speed Induction Motor and Drive in a 7000 Hp Natural Gas Compressor Installation," Proceedings Industry Applications Society 39th Annual Petroleum and Chemical Industry Conference, pp. 141-146.

Melfi, M. J., Rogers, S. D., Evon, S., and Martin, B., 2006, "Permanent Magnet Motors for Energy Savings in Industrial Applications," Proceedings Industry Applications Society 53rd Annual Petroleum and Chemical Industry Conference, pp. 1-8.

Miller T. J. E. and McGilp, M. I., 2004, "PC-BDC 6.5 for Windows—Software," SPEED Laboratory, University of Glasgow, Glasgow, United Kingdom.

Nelson, A., Baker, M., Huynh, C., Hawkins, L., and Filatov, A., 2006, "New Developments in High-speed, Direct-connected, Permanent Magnet Motors and Generators for Marine Applications," in WMTC Conference Record, 2006.

Rosu, M., Arkkio, A., Jokinen, T., Mantere, J., and Westerlund, J., 1999, "Demagnetisation State of Permanent Magnets in Large Output Power Permanent Magnet Synchronous Motor," Electric Machines and Drives, International Conference IEMD '99, pp 776-778.

Say, M. G., 1976, *Alternating Current Machines*, Fourth Edition, John Wiley.

Sebastian, T., Slemon G., and Rahman, M. A., 1986, "Modeling of Permanent Magnet Synchronous Motors," IEEE Transactions on Magnetics, *MAG-22*, (5), pp. 1069-1071.

Shade, N., March 2008, "New Compression and Power Applications," *Compressor Tech Two*, pp. 20-26.

Shanks, G., 1976, "Stator Surface Per Watt (s/w)," Internal Memo to J. Imbertson, February 18.

Steinmetz, C. P., 1984, "On the Law of Hysteresis," Originally Published in 1892 and Reprinted in Proceedings of the IEEE, *72*, pp. 196-221.

Szücs, Á. and Arkkio, A., 1999, "Consideration of Eddy Currents in Multi-Conductor Windings Using the Finite Element Method and the Elimination of Inner Nodes," IEEE Transactions on Magnetics, 35, (3).

Walker, J. H., 1996, *Large Synchronous Machines*, Clarendon Press.

Walter, H., Moehle, A., and Bade, M., 2007, "Asynchronous Solid Rotors as High-speed Drives in the Megawatt Range," Proceedings IEEE Petroleum and Chemical Industry Technical Conference PCIC '07, pp. 1-8.

Weeber, K., Stephens, C., Vandam, J., Yagielski, J., Gravame, A, and Messervey, D., 2007, "High-speed Permanent-magnet Motors for the Oil & Gas Industry," Proceedings of GT2007, ASME Turbo Expo 2007: Power for Land, Sea and Air, Manual Entry.

Wood, B. M., Olsen, C. L., Hartzo, G. D., Rama, J. C., and Szenasi, F. R., 1997, "Development of an 11000-r/min 3500-hp Induction Motor and Adjustable-Speed Drive for Refinery Service," *33*, (3), pp. 815-825.

ACKNOWLEDGMENTS

Special thanks to Paulo Guedes-Pinto and Ladislau Luca for their exceptional work in the design and analysis of the prototype machine discussed herein.